approximately 105 μ the model temperatures at the four locations were greater than when no CO_2 cryodeposits were present. Figure 4 shows that this is to be expected since the reflectance of CO_2 deposit on a black paint substrate is greater than the reflectance of the bare substrate when the deposit thickness exceeds approximately 100 μ. For a deposit thickness of 127 μ, the temperature increases resulting from the increased solar simulator flux reflected to the model are, as seen in Fig. 5a, 16°F on the cylinder bottom, 14°F on the paddle surface, and 8.5°F on the cylinder side. The 6°F temperature increase observed on the cylinder top is a result of the decrease in the energy flux loss from the cylinder top by conduction and internal radiation to the cylinder side and bottom.

Figure 5b presents the changes in the steady-state temperatures obtained at the four representative locations on the test model due to reflection of solar simulator irradiance from various thicknesses of thick (0.146 to 2.51 mm) CO_2 deposits on the floor and wall cryopanels. The changes in the four temperatures rise drastically with thickness due to the increased reflection of solar simulator irradiance by the thicker CO_2 cryodeposits. The greatest increases in temperature with deposit thickness occur on the cylinder bottom and the paddle surface since these two representative model locations have the largest view factor for the solar simulator irradiance reflected directly back toward the vehicle from the floor cryopanel deposits. At location 20 on the cylinder bottom, this temperature increase is as much as 75°F for a deposit thickness of 2.51 mm. Most of this temperature increase, 60°F, occurs for a thickness of 0.78 mm. Figure 5b also shows that a smaller temperature increase occurs at location 5 on the cylinder side (up to 37°F for a 2.51 mm deposit) than on the cylinder bottom and paddle surface locations because the former location does not have a large view factor for the solar simulator irradiance reflected from the floor cryopanel deposits. However, location 5 on the cylinder side does have a large view factor for solar simulator flux reflected from the wall cryopanel deposits. In addition, part of the temperature rise at this location results from an increase in the conduction and radiant energy flux from the cylinder bottom and paddle surface which have an increasingly higher temperature. The smallest temperature rise observed on the model (up to 24°F for 2.51 mm deposit) was at location 2 on the cylinder top. Since the cylinder top is highly reflecting in the spectral range of the solar simulator and also has only a small view factor for solar simulator flux reflected from the wall cryopanel deposits, most of the temperature increase occurring at this location is due to the decrease in the energy flux loss from the cylinder top by internal radiation to the cylinder side and bottom.

Conclusions

The reflection of solar simulator flux from CO_2 cryopanel deposits less than 100 μ thick has only a small effect on the thermal balance of a test article in a space chamber. This effect is not detrimental and the steady-state temperatures of the test vehicle can actually be lower than when there are no CO_2 deposits on the chamber cryopanels. The reflection of solar simulator flux from CO_2 cryopanel deposits of thicknesses greater than 100 μ has a very adverse effect on the thermal balance results for a test model in a space chamber. Most of the increase in test model steady-state temperatures occurs for a deposit thickness of only 0.78 mm.

References

[1] Wood, B. E. and Smith, A. M., "Spectral Reflectance of Water and Carbon Dioxide Cryodeposits from 0.36 to 1.15 μ," *AIAA Journal*, Vol. 6, No. 7, July 1968, pp. 1362–1367.

[2] Seiber, B. A., private communication, July 1969, ARO Inc.

[3] Hsia, H. M., private communication, July 1969, ARO Inc.

Interior Ballistics for Wide-Temperature Throttling of Solid-Propellant Rockets

R. L. H. Lou*

Aerojet-General Corporation, Sacramento, Calif.

Introduction

CONTROLLABLE mass flow rate, or throttling, over a wide temperature range, is one of the principal goals in the current effort to improve the performance and versatility of solid-propellant rockets. To minimize inert weight, the required throttling ratio, $\tau_{req} \equiv (\dot{m}_{max}/\dot{m}_{min})_{req}$ should be accomplished in as low a chamber pressure ratio, $\phi \equiv (P_{max}/P_{min})$, as possible. This, in turn, requires a high burning rate pressure exponent, n, which is limited only by the capability of the control system. Generally, $0.7 \leqslant n \leqslant 0.8$ is considered optimum. For wide-temperature-range operations, typically −65 to 165°F, the temperature sensitivity of equilibrium pressure π_K can significantly increase the pressure ratio required. Thus, π_K should be minimized.

This Note concerns the interior ballistic considerations pertinent to wide-temperature-range throttling by means of a variable-throat-area nozzle. Specifically, the discussion delineates a) the effect of the operating temperature range on the usable throttling ratio, $\tau_u \equiv (\dot{m}_{max}/\dot{m}_{min})_{usable}$, b) the specific temperature/pressure combinations that limit τ_u (and the combinations that do not), and c) the tradeoff between pressure and temperature sensitivity. It is shown that a single parameter, designated the wide temperature throttling exponent, n_T, is useful for rapid screening of the effects of propellant composition and on throttling potential.

Discussion

For simplification and clarity, it is assumed that the pressure and temperature sensitivities of the discharge coefficient are negligible, and that the propellant ballistics can be represented by

$$r = ce^{\pi_p(\Delta T)}P^n \tag{1}$$

at the design temperature, even though these assumptions are not essential to the basic concept advanced. c is an empirical constant whereas T is propellant temperature. Thus, π_K, π_p and n are related by the well known expression:

$$\pi_K = \pi_p/(1 - n) \tag{2}$$

where

$$\pi_K = \left[\frac{\partial \ln p}{\partial T}\right]_K \quad \begin{array}{l}\text{(temperature sensitivity of pressure at}\\ \text{constant } K\text{, propellant burning surface}\\ \text{area to throat area ratio)}\end{array} \tag{3}$$

$$\pi_p = \left[\frac{\partial \ln r}{\partial T}\right]_P \quad \begin{array}{l}\text{(temperature sensitivity of burning rate}\\ \text{at constant pressure)}\end{array} \tag{4}$$

Equation (2) shows that π_K can be reduced by reducing n and/or π_p. Since reducing π_K by reducing n would only lead to a net loss in τ_u for a given ϕ, the only useful approach to reduce π_K for wide temperature throttling is to reduce π_p. A usable throttling ratio (τ_u) for a wide temperature range is the one throttling ratio that can be realized at every point within the temperature range. It is the throttling ratio obtainable at a given temperature (for a given pressure ratio and n) diminished due to the effect of π_p. Furthermore, it will be shown later that only the reductions in π_p at the high T/low P

Received September 11, 1969; revision received December 8, 1969.

* Program Manager, Advanced Technology Programs, Propellant Research and Development Department. Member AIAA.

and at the low T/high P combinations are useful in increasing τ_u.

Figure 1 shows the loss in τ_u due to an increase in operating temperature range. The burning rate/pressure relationship for a propellant at the temperature extremes (T_1 and T_3) and the design temperature (T_2) is shown. Two lines of unit slope are shown which represent K_1 and K_2, respectively, the minimum and maximum ratios of burning surface area to throat area selected due to design constraints such as maximum chamber pressure, minimum stable combustion pressure, minimum throat gap, etc. It is seen that point E represents the minimum achievable $\dot{m}$ and pressure, and point F represents the maximum achievable $\dot{m}$ and pressure. However, the two critical points in Fig. 1 are A and C, because their locations establish τ_u, i.e., the maximum throttling ratio that is achievable at any temperature from T_1 to T_3. Point A represents the maximum $\dot{m}$ achievable at the maximum K at the most adverse (low) operating temperature for high $\dot{m}$, and Point C represents the minimum $\dot{m}$ achievable at the minimum K at the most adverse (high) operating temperature for low $\dot{m}$. The slope of AC here is defined as the "wide-temperature throttling exponent," n_T. This parameter encompasses both the n and temperature sensitivity effects. In other words, the higher the n_T, the lower the pressure ratio required for a given mass flow ratio over a given temperature range.

The relationship of n_T to n and π_p can be derived as follows:

$$n_T = (\ln r_2 - \ln r_1)/(\ln P_2 - \ln P_1) \tag{5}$$

where subscripts 2 and 1 refer to conditions at points A and C, respectively, in Fig. 1
Since

$$\ln r_2 = \ln r_{P_2,T_2} - (T_2 - T_1)\pi_{p_2} \tag{6}$$

and

$$\ln r_1 = \ln r_{P,T_2} + (T_3 - T_2)\pi_p \tag{7}$$

and

$$n = (\ln r_{P_2,T_2} - \ln r_{P_1,T_2})/\ln\phi \tag{8}$$

where

$$\phi = P_2/P_1$$

Substitution of Eqs. (6) and (7) in (5) and simplification lead to

$$n_T = n - [(T_2 - T_1)\pi_{p_2} + (T_3 + T_2)\pi_{P_1}]/\ln\phi \tag{9}$$

where n is the exponent at the design temperature T_2 over the pressure range P_1 to P_2, π_{p_2} is the π_p at P_2 for the temperature range T_1 to T_2, and π_{p_1} is the π_p at p_1 for the temperature range T_2 to T_3. Thus, n_T is a function of n at the design temperature T_2 and of π_p at specific temperature/pressure combinations. Specifically, the only values of π_p of consequence are those at $T_2 \leqslant T \leqslant T_3$ at pressure P_1, and $T_1 \leqslant T \leqslant T_2$ at pressure P_2. (At $T < T_2$ at P_1 or $T > T_2$ at P_2, the π_p is inconsequential, because only the nonlimiting conditions, points B and D in Fig. 1, are influenced).

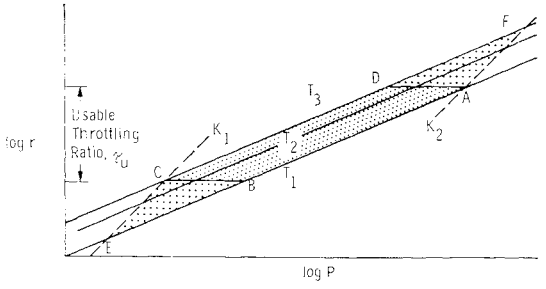

Fig. 1 Effect of wide temperature range on usable throttling ratio τ_u.

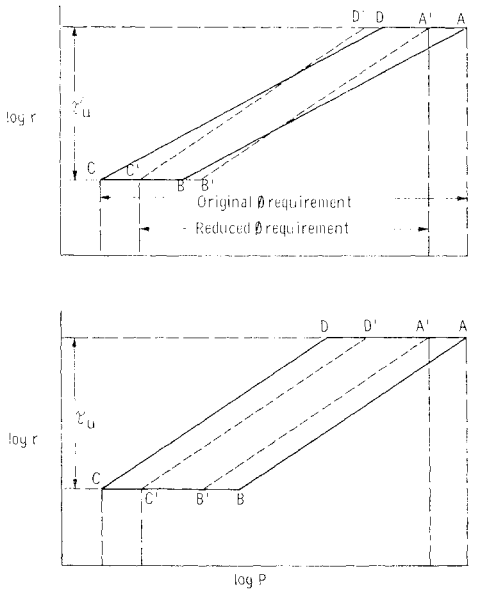

Fig. 2 Effects of n and π_p on τ_u.

It is apparent from Eq. (9) that for positive values of π_p, n_T is lower than n, and the loss due to π_p increases with increasing temperature range and reduced pressure range. For operation at the design temperature only, or for propellants with zero temperature sensitivity, n_T assumes the value of n. If π_p is constant over the temperature and pressure ranges of interest, Eq. (9) reduces to

$$n_T = n - (T_3 - T_1)\pi_p/\ln\phi \tag{10}$$

The effect of increasing n for two propellants with a constant π_p is illustrated in the upper part of Fig. 2. The benefit of a higher n is here shown to be converted into a lower required ϕ for a given throttling ratio. Obviously, the benefit of a higher n may be converted instead into a higher throttling ratio achievable for a given ϕ. Similarly, the effect of reducing π_p for two propellants with a constant n is shown in the lower part of Fig. 2. In each case, the slope of AC or $A'C'$, which is n_T, can be used as a figure of merit for propellant throttlability.

Figure 3 shows the relationship between n_T, n, π_p, and τ_u for ϕ's of interest in a typical application. It is seen that an n_T of 0.65 corresponds to an n of 0.71 with a π_p of 0.001 °F^{-1},

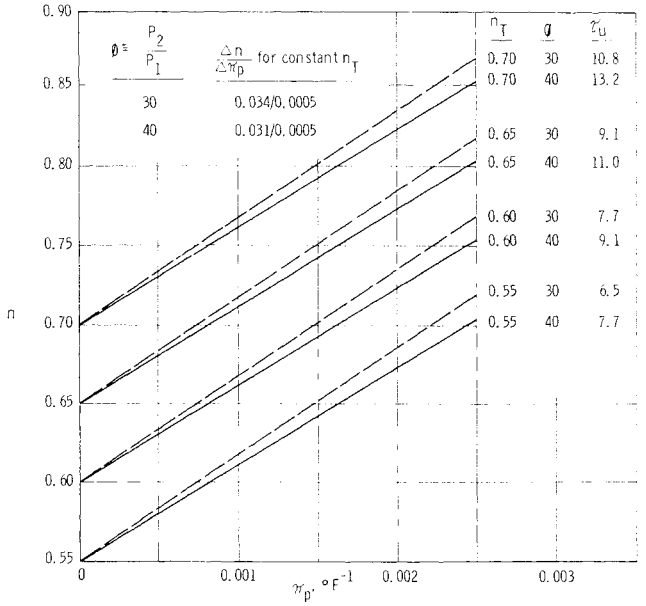

Fig. 3 Relationship between n, π_p and τ_u (ΔT = 230°F).

and will give a τ_u of 11 for a ϕ of 40 over a temperature range of -65 to $+165$°F. Figure 3 also shows that there is probably not much purpose in searching for a π_p reduction of less than $0.0005°F^{-1}$, since it represents an equivalent n increase of only 0.034 and 0.031 for pressure ratios of 30 and 40 respectively. This conclusion provides an opportunity to economize by reducing the number of strands that should be tested for data points to evaluate formulation approaches.

Conclusions

For propellant research and development directed towards an application requiring wide-temperature-range throttling, formulation approaches to reducing π_p need be evaluated principally for their effect between ambient and low temperature at high pressure and between ambient and high temperatures at low pressure. Thus, cost savings may be realized because π_p need not be determined over the entire temperature range at all pressures. Because n_T is the controlling parameter for propellant throttlability it is advantageous economically to determine n_T directly instead of indirectly by determining n and π_p values.

Temperature Distribution in Shadowed Lunar Craters

A. S. ADORJAN*
General Electric Company, Houston, Texas

Nomenclature

A = surface area of crater, ft²
A_0 = total surface area of sphere, ft²
A_D = surface area of circle by the intersection of the sphere and the lunar surface, ft²
a = D/h, aspect ratio of crater, diameter/depth
F_{ij} = form factor relating A_i and A_j
J = radiosity at an arbitrary location, Btu/hr-ft²
K_{ij} = kernel of Fredholm's integral equation or normalized form factor in the heat balance equations
$\mathbf{n}$ = crater surface unit normal vector
q = local incident heat flux, Btu/hr-ft²
R = radius of sphere, ft
$\mathbf{S}$ = solar constant, 442 Btu/hr-ft²
$\mathbf{s}$ = solar ray directional unit vector
T = radiation equilibrium temperature, °R
α, ϵ = absorptivity and emissivity of lunar soil
γ = thermal inertia of lunar soil, 750 cm²-sec$^{\frac{1}{2}}$-°C/cal
δ = solar elevation angle
λ = parameter of the integral equation
σ = Stefan-Boltzmann constant, 0.1714×10^{-8} Btu/hr-ft²-°R⁴

Subscripts

1, 2 = sunlit and snadowed regions of crater
s = source

Introduction

AN interest in temperature distribution of lunar topographical features has existed for many years. However, most of the experimental (e.g., Ref. 1) and analytical (e.g., Ref. 2) efforts, limited by the resolution of Earth-based instrumentation, have been concentrated on average temperatures of relatively large surface areas. More detailed experimental data have been obtained by the Surveyor flights, especially by Surveyor III and V.[3,4] Lunar surface temperatures were obtained, however, by indirect methods (through compartment temperature data) limiting the accuracy of results. Furthermore, the crater in which Surveyor III landed was too shallow to exhibit marked "cavity" effect. Significant results have been obtained, however, on the thermal inertia of the lunar soil, indicating a numerical value of 500 cm²-sec $\frac{1}{2}$-°C/cal instead of 750 used previously based on terrestrial measurements.

The present study considers temperature distribution in lunar craters. The governing equations of the heat balance are defined in a set of integral equations. Independent of the depth of the crater, the incident solar radiation is identical for all craters with the same surface area at their openings. By energy consideration, the emitted radiation must also be the same. Consequently, heat emission from deep craters may occur at higher surface temperatures in order to compensate for the decrease in the form factor from the cavity toward the deep space.

To simplify the analysis, it is assumed that $\epsilon = 1$ (corresponding closely to the experimental data) and that $\alpha = 1$ instead of the usual 0.93. Uncertainties of local albedo values and especially gross assumptions on the surface contour of the crater may introduce larger errors than the second assumption. In addition, reabsorption from the first and higher order reflections of the incident radiation may result in an effective α significantly higher than 0.93.

Analysis

In Fig. 1 incident heat flux at A_j from the sun and subsurface sources is

$$q_j = S_j + q_{sj} \tag{1}$$

and radiation leaving surface dA_i which is absorbed at surface dA_j is

$$dA_j q_{ij} = dA_i dF_{ij} J_i \tag{2}$$

The reciprocity relation states that

$$dA_i dF_{ij} = dA_j dF_{ji} \tag{3}$$

Combining Eqs. (2) and (3),

$$q_{ij} = J_i dF_{ji} \tag{4}$$

Furthermore, the diffuse form factor can be expressed as

$$dF_{ji} = K_{ji} dA_i \tag{5}$$

then

$$J_i dF_{ji} = K_{ji} dA_i J_i \tag{6}$$

where K_{ji} is the normalized form factor. The radiosity at A_j can be expressed as the sum of Eq. (1) and the contribution of radiation originated from all dA_i elements, which is the integral of Eq. (6) over the total crater surface:

$$J_j = q_j + \int_A K_{ji} J_i dA_i \tag{7}$$

This relation is Fredholm's integral equation of the second kind, which, in mathematical notation is

$$y(x) = f(x) + \lambda \int_a^b K(x, t) y(t) dt \tag{8}$$

where $y(x)$ is the unknown function (here, the radiosity of the

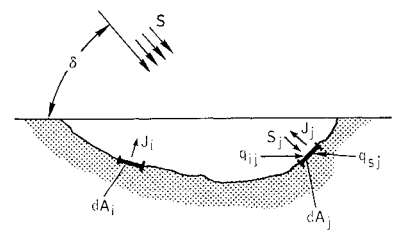

Fig. 1 Model of lunar crater for the heat balance equations.

Presented as Paper 69-595 at the AIAA Fourth Thermophysics Conference, San Francisco, Calif., June 16–18, 1969; submitted October 20, 1969; revision received December 22, 1969. The study was conducted for NASA by General Electric under Contract NASw-410.

* Consulting Engineer, Apollo Systems. Member AIAA